# Supplementary Material to 'Vacancy-ordering-induced topological Hall effect in Zintl $Eu_2ZnSb_2$'

Zan Du, Azizur Rahman, Yihao Wang, Jiangpeng Song, Wei Liu, Min Ge, Chunlan Ma, Jiyu Fan, Li Pi, Yimin Xiong, Lei Zhang, and Yuheng Zhang

### A. Experimental details

Starting materials Eu (99.9%), Zn (99.95%), Sb (99.99%), and Sn (99.9%) were mixed in Ar-filled glove box at a molar radio of Eu : Zn : Sb : Sn = 2 : 1 : 2 : 10. The mixture was placed in a 2 mL alumina crucible sealed in an evacuated quartz tube. The tube was heated up to 1000 °C in 500 minutes in a furnace, and dwelt for 1 day. Then the tube was cooled down slowly to 500 °C at a rate of 3 °C/h. At this temperature, the crystals were separated from molten Sn flux by centrifuging. Finally, shiny hexagonal crystals were obtained on the bottom of the crucible.

The crystalline structure was characterized by X-ray diffraction (XRD) with Cu K$\alpha$ radiation using Rigaku-TTR3 diffractometer. The chemical compositions of selected crystals were analyzed by an energy dispersive x-ray (EDX) spectrometry in an FEI Nanolab 600i SEM/FIB dual beam system. A vibrating sample magnetometer (VSM) with superconductive quantum interference device (SQUID) was used to measure the magnetic properties (MPMS-3, Quantum Design). The electric transport measurements were carried out in Oxford Instrument Teslatron-PT cryogenic system and Quantum Design Physical Property Measurement System (PPMS). Standard six-terminal method was used in order to measure the transport properties with the current flowing in the *ab*-plane.

### B. XRD and EDX

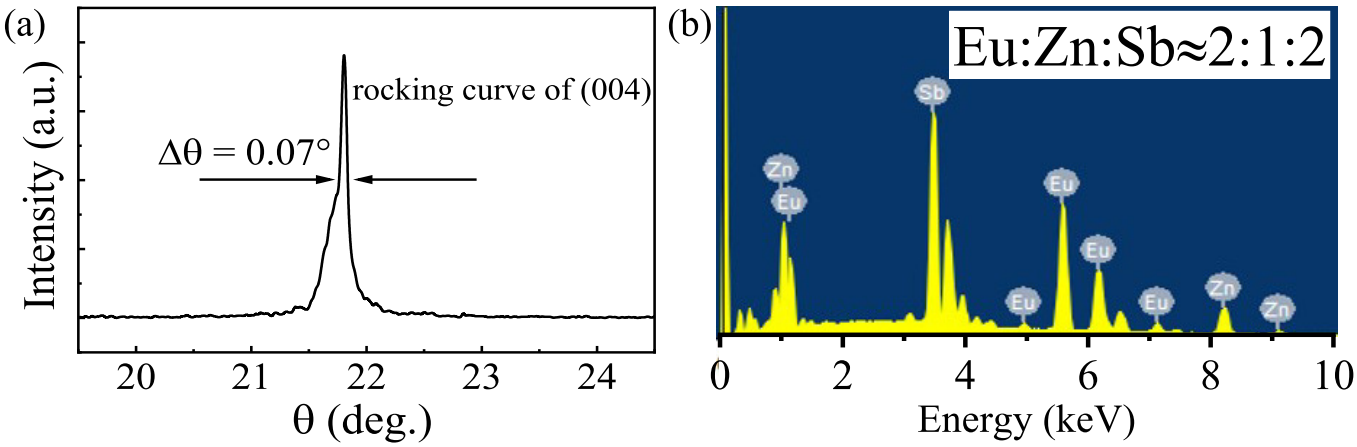


Fig. S 1. (a) The rocking curve of (004) reflection. (b) The EDX spectrum of $Eu_2ZnSb_2$ single crystal.

As shown in Fig. S1 (a), the rocking curve of (004) reflection displays a single peak shape. The single peak and small full-width-at-half-maxium (FWHM) $\Delta\theta = 0.07°$ indicates the high quality of the as-grown single crystals. Table SI display the EDX results of different samples. Only three elements of Eu, Zn, Sb are observed and the element ratio is close to 2 : 1: 2, which prove the as-grown crystals are the objective chemical constituents of $Eu_2ZnSb_2$. The EDX spectrum of $Eu_2ZnSb_2$ single crystals show that the element ratio of Eu, Zn, and Sb is close to 2 : 1 : 2, as displayed in Fig. S1 (b). A slightly deviation of practical ratio of Eu element from 2 indicate the existence of a small amount of Eu vacancies in our samples.

The XRD refinement results of three insulator-models are shown in Fig. S2 (a)-(c). The large difference between experiment data and theoretical fitting curve suggests that the insulator-vacancy-models are not suitable for our samples, which is consistent with the semi-metal electric-transport behaviors.

TABLE I. The EDX results measured in different samples. The relative content of Eu element and Zn element are based on the content of Sb element.

| Composition | Eu | Zn | Sb |
|---|---|---|---|
| Sample1 | 1.93 | 1.01 | 2 |
| Sample2 | 1.85 | 0.98 | 2 |
| Sample3 | 1.84 | 0.97 | 2 |

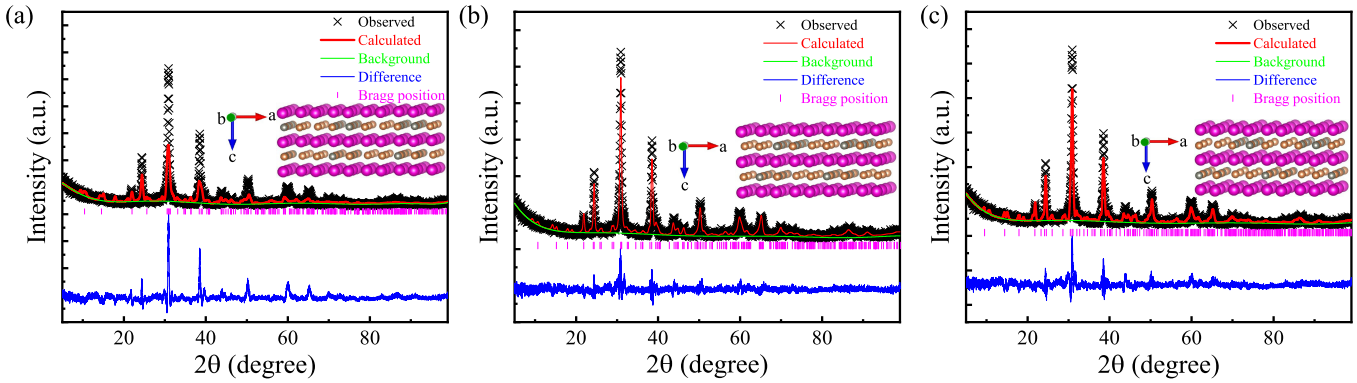


Fig. S 2. (a) XRD refinement based on armchair Zn-Sb chain model-III (insulator vacancy type-III); (b) armchair Zn-Sb chain model-IV (insulator vacancy type-IV); (c) armchair Zn-Sb chain model-V (insulator vacancy type-V). The insets display the vacancy structure of three models respectively.

### C. Magnetization

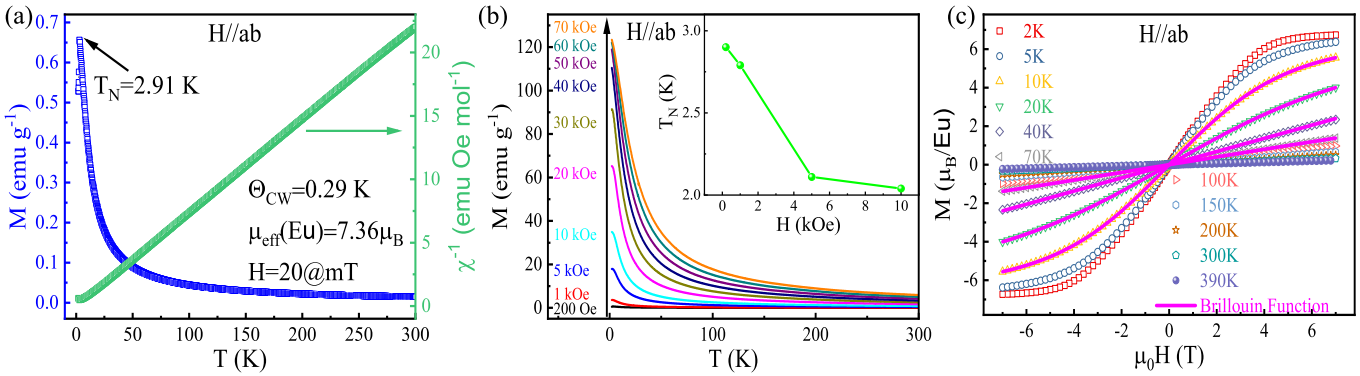


Fig. S 3. (a) Temperature dependence of magnetization $[M(T)]$ (left-axis) and reciprocal of susceptibility $[\chi^{-1}(T)]$ (right axis) for $H//ab$. (b) $M(T)$ curves under variable applied magnetic field from 200 Oe to 70 kOe. (c) $M(H)$ at different temperatures (the purple curves represent the Brillouin function fitting).

The temperature dependence of magnetization $[M(T)]$ (left-axis) with $H = 20$ mT and reciprocal of susceptibility $[\chi^{-1}(T)]$ (right axis) for single-crystal $Eu_2ZnSb_2$ with $H//ab$ are displayed in Fig. S3 (a). The determined antiferromagnetic (AFM) phase transition temperature $T_N$ is about 2.91 K. The $M(T)$ curve in paramagnetic (PM) state above $T_N$ can be fitted by the Curie-Weiss law $\chi = C/(T-\Theta_{CW})$ (where $C$ is Curie constant with $C = N\mu_{eff}^2 J(J+1)/3k_B$, $N$ is the number of magnetic atoms per unit volume, and $\mu_{eff}$ is the effective atomic moment). The obtained Curie-Weiss temperature $\Theta_{CW}$ is 0.29 K, and the calculated effective atomic moment is 7.87 $\mu_B$. With the increase of field, the AFM transition shifts towards lower temperature direction, and then vanish gradually. The inset of Fig. S3 (b) plots the field-dependent $T_N$, indicating the absolute suppression of the AFM phase beyond 2 T. Figure S3 (c) depicts

the field-dependent magnetization $[M(H)]$ at different temperatures. With the increase of field, the magnetization tends to saturation at $T = 2$ K, and the saturation moment is 7.03 $\mu_B$ at 7 T. The $M(H)$ curves above $T_N$ at different temperatures can be fitted by the Brillouin function. The magnetization behavior for $H//ab$ is highly similar with that for $H//c$, which suggest the weak magnetic anisotropy.

### D. Resistivity

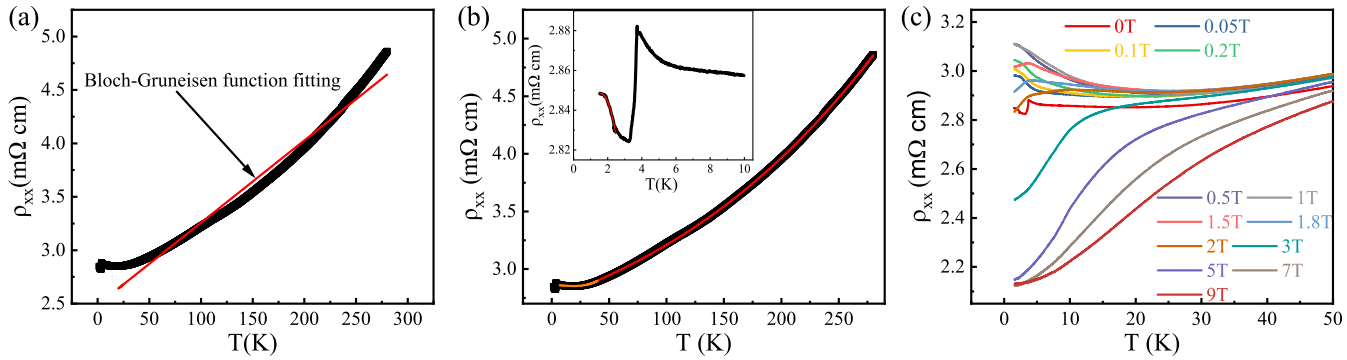


Fig. S 4. (a) The comparison between $\rho_{xx}(T)$ and the fitting results based on Bloch-Gruneisen model. (b) The $\rho_{xx}(T)$ with the current flow along $ab$-plane ($I//ab$). The fitting results at varying temperature zone are represented by the red and blue line. The inset show the enlargement of $\rho_{xx}(T)$ below 10 K. (c) The raw curves of resistivity under different applied fields below 50 K.

For general metals or semi-metals, the temperature-dependent longitudinal resistivity is dominated by electron-phonon interaction and can be described by the Bloch-Grüneisen (BG) model. The BG model can be expressed as:

$$\rho_{xx}(T) = \rho_0 + C(\frac{T}{\Theta_D})^5 \int_0^{\Theta_D/T} \frac{x^5}{(e^x - 1)(1 - e^{-x})} dx \tag{1}$$

where the $\rho_0$ is the residual resistivity due to defect or impurity scattering, and $\Theta_D$ is the Debye temperature. However, the $\rho_{xx}(T)$ of $Eu_2ZnSb_2$ cannot be fitted by BG model, as shown in Fig. 4 (a) This difference between them imply that complicated scattering mechanisms exist in this system. According to the Rivier-Zlatic model of local spin fluctuation (LSF), the $\rho(T)$ varies as $T^2$ at low temperatures ($\rho \propto T^2$), and changes gradually to a linear dependence on $T$ when approaching $\Theta_{SF}$ ($\rho \propto T$) ($\Theta_{SF}$ is the spin-fluctuation characteristic temperature) [1, 2]. The model is not only appropriate to transition metal based on $3d$-electron systems, but also to those on $f$-electron systems [1–4]. Therefore, we consider that the $\rho(T)$ contributed by the AFM fluctuation satisfies the $T^2$ dependent relationship in the low temperature region, while $T$ dependence in the high temperature region ($T < \Theta_{SF}$). Furthermore, if the lifetime of FM fluctuation is longer than the time of inelastic scattering of carriers from local magnetic moments, the scattering effect on the carriers is equivalent to that from local magnetic moment in the ferromagnetic (FM) state. The resistivity is proportional to $T^{2.5}$ in FM state [5]. Hence, the contribution from FM fluctuation can be expressed as $T^{2.5}$. The expression including AFM fluctuation and FM fluctuation contribution is constructed to fit the $\rho_{xx}(T)$ curve as follow:

$$\begin{aligned} \rho_{xx}(T) &= \rho_0 + A_1 T^2 + B_1 T^{2.5}, \ T < 40K \\ \rho_{xx}(T) &= \rho_0 + A_2 T + B_2 T^{2.5}, \ 40K < T < 300K \end{aligned} \tag{2}$$

The $A_i$ and $B_i$ ($i = 1, 2$) are fitting parameters. The fitting well agrees the experiment results, as shown in Fig. S4 (a). The raw curves of $\rho_{xx}(T)$ under variable applied field are shown in Fig. S4 (b).

### E. Magnetoresistance

The magnetoresistance (MR) can also be fitted well by AFM and FM fluctuation model. The MR contributed by AFM fluctuation is proportional to $H^{1.5}$[2], while that from FM fluctuation have different relationship, dependent on

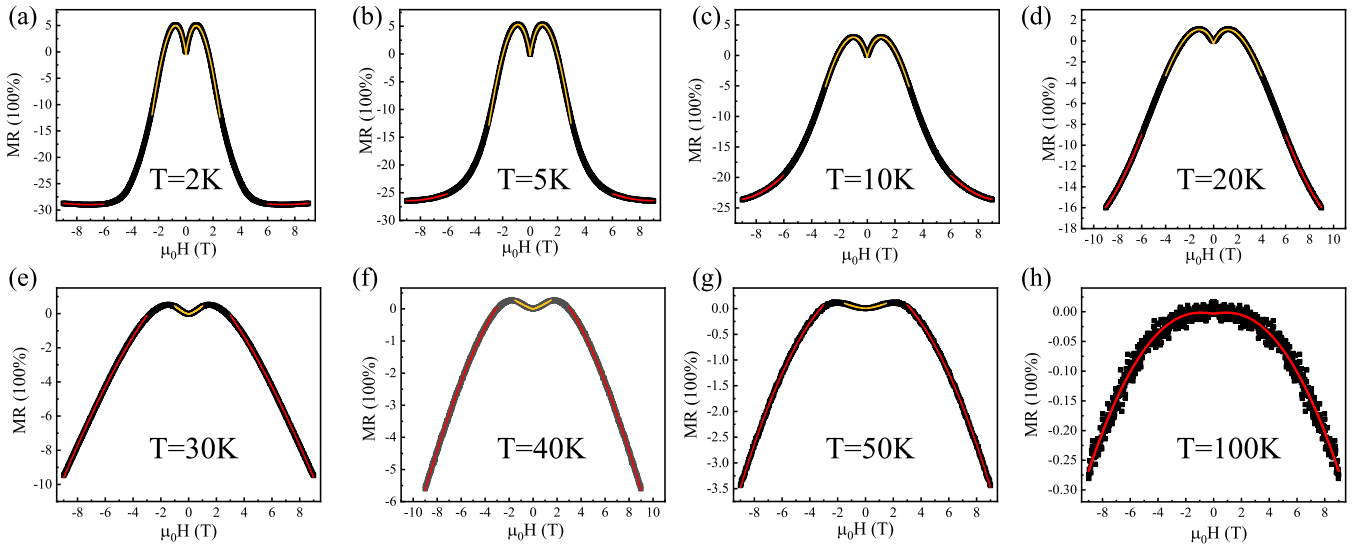


Fig. S 5. Field-dependent magnetoresistance (MR) with $H//c$ and $I//ab$ at (a) $T = 2$ K, (b) $T = 5$ K, (c) $T = 10$ K, (d) $T = 20$ K, (e) $T = 30$ K, (f) $T = 40$ K, (g) $T = 50$ K, (h) $T = 100$ K.

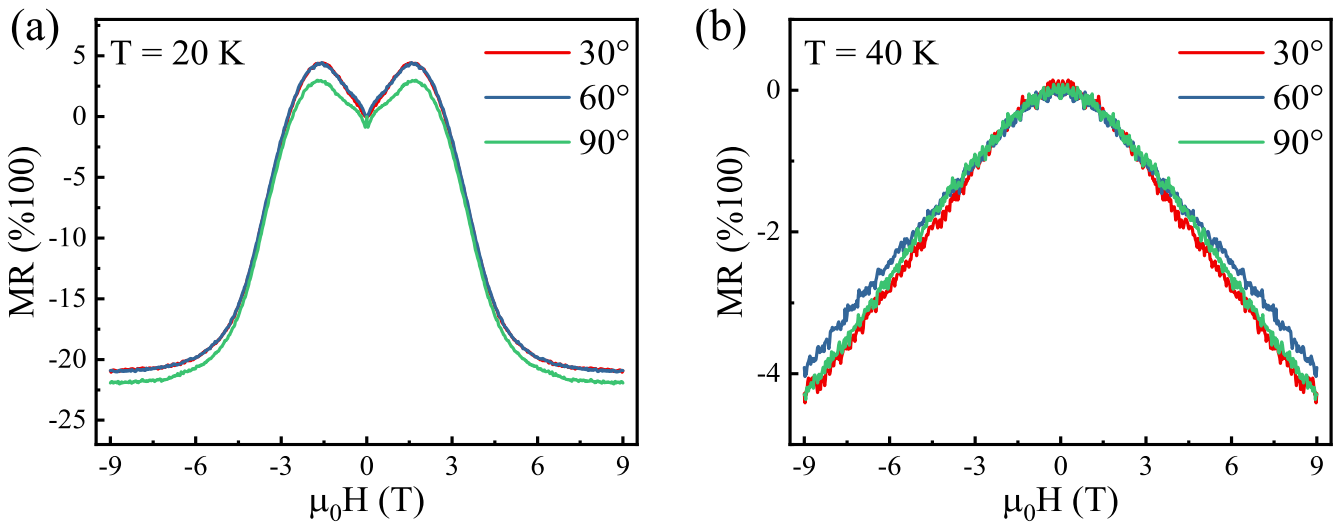


Fig. S 6. Angle-resolved MR with angles at $\theta = 30°, 60°, 90°$ between the field direction and the $c$-axis at (a) $T = 20$ K and (b) $T = 40$K.

$H$ in low field (LF) region and $H^2$ in high field (HF) region [6]. Hence, the MR curves at different temperatures can be fitted by the following equations:

$$\begin{aligned} MR &= a_1 H^{1.5} + b_1 H, LF \\ MR &= a_2 H^{1.5} + b_2 H^2, HF \end{aligned} \tag{3}$$

The $a_i$ and $b_i$ $(i = 1, 2)$ are fitting parameters. The yellow line represents the fitting curve by $a_1 H^{1.5} + b_1 H$, while the red line represents the fitting curve by $a_2 H^{1.5} + b_2 H^2$. The experimental curves are fitted well by Eqs. 3, as shown in Fig. S5. Note that, with the increasing of temperature, the linear relationship with $H$ contributed by FM fluctuation in low field region is gradually weak, corresponding to the reduction of the fitted range of the yellow line. In contrast, the fitted range of the red line gradually increase, suggesting that the dependence relationship between MR contributed by FM fluctuation and $H$ is gradually unified as $H^2$. When $T = 100$ K, the MR can be fitted by $a_2 H^{1.5} + b_2 H^2$ over the whole field range. The quantitative fittings of MR further prove that the AFM and FM fluctuations coexist in this system.

Figure S6 shows the angle-resolved MR curves at $T = 20$ K and $T = 40$ K, which also indicate the weak anisotropy of MR, consistent with magnetization behaviors.

### F. Anomalous Hall effect

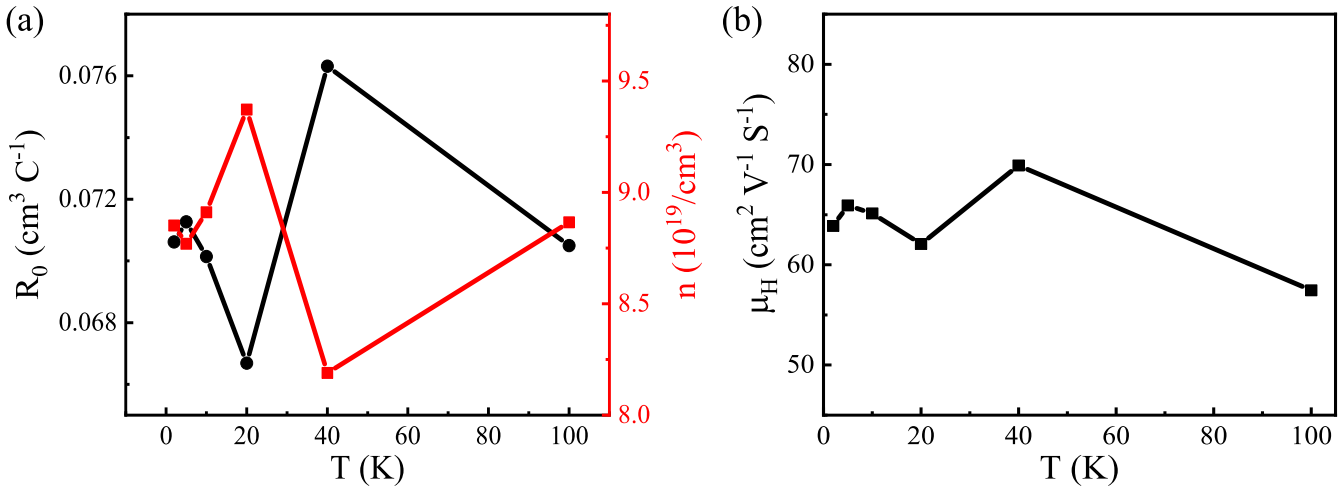


Fig. S 7. (a) The normal Hall coefficient (in the left axis) and carrier concentration (in the right axis); (b) The carriers mobility at various temperatures (below 100 K).

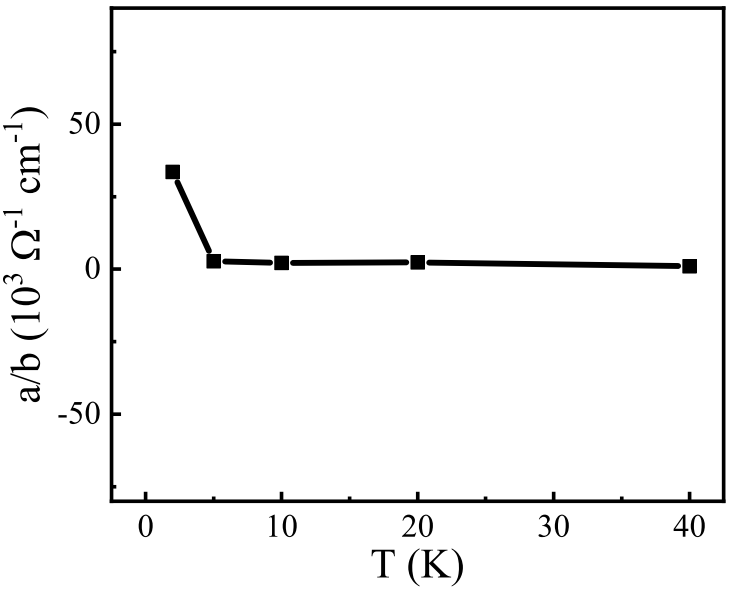


Fig. S 8. The ratio of fitting parameter (*i.e.* $a/b$) from different anomalous Hall mechanisms at various temperatures ($a$ and $b$ are from $a\rho_{xx}^2 M + b\rho_{xx} M$, $\rho_{xx}^2 M$ and $\rho_{xx} M$ correspond to the intrinsic mechanism and skew scattering mechanism respectively).

Figure S7 (a) shows the temperature dependence of the obtained normal Hall coefficient $R_0$ in the left-axis and carrier concentration $n$ in the right-axis below $T = 100$ K, which reveals the weak temperature-dependence $R_0$ and $n$. The order of magnitude of $n$ is $1{\times}10^{19}$/cm$^3$, suggesting the bad-metal characteristic of $Eu_2ZnSb_2$ single crystal. The carriers mobility $\mu_H$ have no obvious variation as increasing temperature, as shown in Fig. S7 (b).

Considering the contribution from intrinsic and extrinsic mechanisms, the model combining them (*i.e.* $a\rho_{xx}^2 M + b\rho_{xx} M$) is constructed to describe the anomalous Hall resistivity. The $a/b$ represents the extent of contribution

from intrinsic and extrinsic mechanism. Fig. S8 displays the temperature-dependent ratios $a/b$, which is about the magnitude of $1\times10^3\sim1\times10^4$. This result reveals that the dominated anomalous Hall mechanism in this system is intrinsic one (*i.e.* KL mechanism). However, in order to more accurately extract the topological Hall resistivity, we also subtract the contribution from Skew mechanism.


[1] N. Rivier and V. Zlatic, J. Phys. F: Metal Phys. **2**, L87 (1972).
[2] M. Chattopadhyay, P. Arora, and S. Roy, J. Phys. Condens. Matter **24**, 146004 (2012).
[3] A. Kaiser, Philos. Mag. B **65**, 1197 (1992).
[4] Z. Altounian, S. V. Dantu, and M. Dikeakos, Phys. Rev. B **49**, 8621 (1994).
[5] V. Sen, N. Panwar, G. Bhalla, and S. Agarwal, J. Phys. Chem. Solids **68**, 1685 (2007).
[6] S. N. Kaul, J. Phys. Condens. Matter **17**, 5595 (2005).